

Identification of candidate millisecond pulsars from *Fermi* LAT observations II

Xue-Jie Dai^{1,2}, Zhong-Xiang Wang¹, Jithesh Vadakkumthani¹ and Yi Xing¹

¹ Shanghai Astronomical Observatory, Chinese Academy of Sciences, Shanghai 200030, China;
wangzx@shao.ac.cn

² University of Chinese Academy of Sciences, Beijing 100049, China

Received 2016 December 5; accepted 2017 April 5

Abstract On the basis of the properties of known γ -ray millisecond pulsars (MSPs), we have selected 77 un-associated sources from the Fermi Large Area Telescope (LAT) third source catalog for the purpose of finding likely candidate MSPs. Previously, detailed LAT data analysis for 39 of them was reported, and here we report the analysis for the remaining 38 sources. We identify that among the 38 sources, 28 of them are single point-like sources with clean background and their spectra show significant curvature. We also conduct an analysis of archival X-ray data available for 24 of the 28 sources. In the fields of 10 sources, there is at least one X-ray object, and in those of the other 14 sources, no X-ray object is detected but this is probably due to the X-ray observations being short. We discuss the possible MSP nature for these sources. Six of them (J0514.6–4406, J1035.7–6720, J1624.2–4041, J1744.1–7619, J1946.4–5403 and J2039.6–5618) are most likely associated with pulsars because of multi-wavelength identifications including direct radio or γ -ray detection of pulsations. To firmly establish the associations or verify the MSP nature for other sources, deep X-ray and/or optical observations are needed.

Key words: stars: pulsars — stars: binaries — gamma rays: stars

1 INTRODUCTION

The launch of the *Fermi* Gamma-Ray Space Telescope (*Fermi*) in 2008 June marked a new era in γ -ray astronomy. With its unprecedented capabilities, the Large Area Telescope (LAT) onboard *Fermi* has allowed us to, for the first time, find large numbers of different classes of γ -ray sources in the sky and study their properties in detail. Using the first four-years (2008–2012) of all-sky monitoring data obtained with LAT, more than 3000 sources in the energy range of 0.1–100 GeV have been found (Acero et al. 2015). Classification studies of these sources, which are listed in the *Fermi* LAT third source catalog (3FGL), have confirmed results from the surveys of the sky with previous gamma-ray telescopes, e.g., the *Compton Gamma-Ray Observatory*: the dominant class of extragalactic γ -ray sources is active galactic nuclei (AGNs; Ackermann et al. 2015a) and in the Milky Way, pulsars are the majority (Abdo et al. 2013; Acero et al. 2015).

From *Fermi* LAT observations of pulsars, it has been learned that they have stable γ -ray emission and their spectra can generally be described by a power law (PL) with an exponential cutoff (Abdo et al. 2013). Such spectral properties match the theoretical expectations well for high-energy emission mechanisms of pulsars (e.g., Muslimov & Harding 2004), and can be used for finding new candidate pulsars among the nearly 1000 3FGL sources that have not been found to be associated with any known types of high-energy objects (Acero et al. 2015). Currently more than 200 γ -ray pulsars have been identified¹, and among them more than 20 are newly discovered millisecond pulsars (MSPs). The discoveries of a significant number of new MSPs were made due to *Fermi* LAT's first detection of them, so that follow-up radio and other wavelength observations could be carried out for identification.

For the purpose of finding new MSPs, we have conducted a systematic study of un-associated 3FGL

¹ <https://confluence.slac.stanford.edu/display/GLAMCOG/Public+List+of+LAT-Detected+Gamma-Ray+Pulsars>

sources. We have selected 101 sources from 3FGL, requiring their properties to be non-variable with curved spectra and having Galactic latitudes of $>5^\circ$ (Dai et al. 2016; hereafter paper I). There were 24 sources with a low detection significance (average_sig $< 6\sigma$; Acero et al. 2015). No data analysis was conducted for the 24 sources because of their low detection significance: the low photon counts do not allow us to clearly determine their properties. For the remaining 77 sources, their *Fermi* LAT data were analyzed. From the analysis, those contaminated by extended background emission or mixed with nearby unknown sources were excluded. Further selection was conducted on the basis of the spectra we obtained. In this way, we were able to find ‘good’ candidate MSPs for follow-up identification. In Paper I, we reported our target selection, and because a large amount of computing time was required for *Fermi* data analysis, the detailed LAT data analysis for 39 of them was presented. The sources are mostly in the Northern Hemisphere, and, among them, we were able to find 24 that are possible candidate MSPs (which were thus taken as targets for our follow-up observation program conducted with optical telescopes). In this paper, we report our data analysis for the other 38 sources that are in the Southern Hemisphere.

2 *Fermi* LAT DATA ANALYSIS

2.1 *Fermi* LAT Data

LAT onboard *Fermi* is an instrument generally carrying out an all-sky survey in the energy range from 20 MeV to 300 GeV. With its wide field-of-view and high sensitivity, γ -ray events are distinguished from background events through measuring the direction, energy and arrival time of each γ -ray photon (Atwood et al. 2009). In our data analysis, we used the latest Pass 8 data, which were acquired from 2008 August 4 15:43:39 to 2015 October 22 00:26:36 (UTC). We extracted data within 15° of a target’s position in the energy range from 200 MeV to 300 GeV, for which photons below 200 MeV were not included to avoid the relatively large uncertainties of the instrument response function for LAT in the low energy range. In addition, as recommended by the LAT team, we selected events with zenith angles less than 90° to exclude possible contamination from Earth’s limb.

2.2 Maximum Likelihood Analysis

Using the newly released LAT science tools package v10r0p5, we performed a standard binned maximum likelihood analysis (Mattox et al. 1996) on the data of each target. In a source model for a target,

all sources within the 20° region were included. The spectral parameters of these sources are provided in 3FGL, and the spectral normalization parameters of those within 5° from each target were set free and all the other parameters were fixed at their catalog values. For Galactic and extragalactic diffuse emission, we included the model gll_iem_v06.fits and spectrum file iso_P8R2_SOURCE_V6_v06.txt in the source model. The normalization parameters of the two diffuse emission components were left free.

We obtained the Test Statistic (TS) map of a $2^\circ \times 2^\circ$ region centered at the position of each target. TS values are calculated from $TS = -2 \log(L_0/L_1)$, where L_0 and L_1 are the maximum likelihood values for a model without and with an additional source at a specified location respectively (Abdo et al. 2010). The TS value for a given source is approximately the square of the detection significance. We examined the TS map of each target, and selected ‘clean’ sources among the targets, which we defined to be point-like sources, not mixed with other unknown sources and/or not in a region with strong extended emission (see examples in Paper I). We were able to find 29 sources that are such clean sources. They are listed in Tables 1 and 2. We then ran *gfindsrc* in the LAT software package to determine the positions of these 29 sources. The best-fit positions we obtained are consistent with those provided in 3FGL within 2σ error circles.

The other nine sources, which were found not to be clean point-like sources, were excluded from our target list. For them, further data analysis to determine their properties would require a large amount of computing time. Their spectral parameters in 3FGL are provided here in Table 3. Among them, six sources were fitted with a PL model,

$$\frac{dN}{dE} = N_0 E^{-\Gamma} \quad , \quad (1)$$

where N_0 and Γ are the normalization and photon index, respectively. The other three sources were fitted with a LogParabola model,

$$\frac{dN}{dE} = N_0 \left(\frac{E}{E_b} \right)^{-\alpha - \beta \log(E/E_b)} \quad , \quad (2)$$

where N_0 , α and β are flux density, photon index and curvature, respectively. The energy E_b was set such that errors on differential fluxes were minimal and the ‘‘Signif_curve’’ (in Table 3) is the curvature significance estimated from likelihood values for a PL model or a LogParabola model.

Table 1 Spectral Results for 28 Candidate MSPs

Source name	Spectral model	Flux	Γ	E_c	TS	Signif_Curve (σ)	Comments
		(10^{-9} photon $\text{cm}^{-2} \text{s}^{-1}$)		(GeV)			
J0048.1–6343	PowerLaw	1.5 ± 0.3	2.1 ± 0.1		87	3.48	
	PLSuperExpCutoff	0.8 ± 0.3	0.7 ± 0.9	2 ± 2	98		
J0514.6–4406	PowerLaw	5.9 ± 0.5	2.58 ± 0.07		261	7.72	c-MSP
	PLSuperExpCutoff	4.3 ± 0.6	0.5 ± 0.5	0.5 ± 0.1	315		
J0802.3–5610	PowerLaw	9.0 ± 0.7	2.39 ± 0.06		332	7.10	
	PLSuperExpCutoff	7.3 ± 0.7	1.4 ± 0.2	1.5 ± 0.4	382		
J0838.8–2829	PowerLaw	7.3 ± 0.6	2.58 ± 0.07		482	5.11	
	PLSuperExpCutoff	5.8 ± 0.6	1.6 ± 0.1	6 ± 2	506		
J0933.9–6232	PowerLaw	10.1 ± 0.6	2.03 ± 0.04		842	12.72	c-MSP N
	PLSuperExpCutoff	6.0 ± 0.6	0.6 ± 0.2	1.9 ± 0.3	996		
J0954.8–3948	PowerLaw	15.6 ± 0.8	2.60 ± 0.05		696	4.26	
	PLSuperExpCutoff	14.7 ± 0.9	2.2 ± 0.1	4 ± 1	712		N
J1035.7–6720	PowerLaw	18.7 ± 0.3	2.19 ± 0.01		1493	12.84	c-MSP
	PLSuperExpCutoff	14.4 ± 0.8	1.3 ± 0.1	2.2 ± 0.3	1637		
J1119.9–2204	PowerLaw	17.2 ± 0.7	2.24 ± 0.03		2114	12.57	c-MSP c-subhalo
	PLSuperExpCutoff	13.7 ± 0.7	1.3 ± 0.1	1.7 ± 0.2	2262		
J1231.6–5113	PowerLaw	13.8 ± 0.9	2.70 ± 0.06		461	6.25	
	PLSuperExpCutoff	12.0 ± 0.9	1.7 ± 0.2	1.1 ± 0.3	492		
J1400.2–2413	PowerLaw	3.4 ± 0.5	2.15 ± 0.08		169	5.95	
	PLSuperExpCutoff	1.8 ± 0.2	0.7 ± 0.4	1.7 ± 0.5	204		
J1539.2–3324	PowerLaw	6.5 ± 0.5	1.89 ± 0.04		581	12.35	c-AGN N
	PLSuperExpCutoff	3.5 ± 0.4	0.4 ± 0.2	2.2 ± 0.3	733		
J1544.1–2555	PowerLaw	7.9 ± 0.7	2.36 ± 0.06		265	6.17	
	PLSuperExpCutoff	6.1 ± 0.7	1.5 ± 0.2	2.2 ± 0.6	300		
J1624.2–4041	PowerLaw	27 ± 1	2.36 ± 0.03		1049	9.61	c-MSP
	PLSuperExpCutoff	19.7 ± 0.9	1.58 ± 0.04	2.8 ± 0.1	1082		
J1626.2–2428c	PowerLaw	26 ± 3	2.50 ± 0.05		587	3.17	c-AGN N
	PLSuperExpCutoff	23 ± 3	2.3 ± 0.1	10 ± 5	542		
J1645.7–2149	PowerLaw	10 ± 1	2.54 ± 0.07		176	3.68	
	PLSuperExpCutoff	9 ± 1	1.9 ± 0.3	2 ± 1	188		
J1649.6–3007	PowerLaw	7.1 ± 0.8	2.24 ± 0.06		208	6.23	
	PLSuperExpCutoff	4.2 ± 0.8	1.2 ± 0.3	2.6 ± 0.7	244		
J1702.8–5656	PowerLaw	34 ± 1	2.53 ± 0.03		2209	6.65	
	PLSuperExpCutoff	32 ± 1	2.21 ± 0.07	5 ± 1	2228		N
J1744.1–7619	PowerLaw	18.5 ± 0.7	2.15 ± 0.03		2023	14.72	c-MSP
	PLSuperExpCutoff	13.6 ± 0.8	1.1 ± 0.1	1.9 ± 0.2	2211		
J1753.6–4447	PowerLaw	7.5 ± 0.7	2.24 ± 0.06		250	6.10	
	PLSuperExpCutoff	5.0 ± 0.7	1.2 ± 0.3	2.1 ± 0.6	286		
J1757.7–6030	PowerLaw	2.6 ± 0.4	2.00 ± 0.08		160	5.14	
	PLSuperExpCutoff	1.2 ± 0.3	0.8 ± 0.4	4 ± 1	187		
J1808.3–3357	PowerLaw	10 ± 1	2.43 ± 0.06		186	7.39	
	PLSuperExpCutoff	6.9 ± 0.8	1.1 ± 0.2	1.3 ± 0.2	237		
J1831.6–6503	PowerLaw	3.2 ± 0.4	2.08 ± 0.07		177	6.12	
	PLSuperExpCutoff	1.7 ± 0.4	0.6 ± 0.4	2.0 ± 0.7	213		
J1946.4–5403	PowerLaw	8.9 ± 0.5	2.20 ± 0.04		795	11.49	c-MSP
	PLSuperExpCutoff	6.2 ± 0.5	0.8 ± 0.2	1.3 ± 0.2	927		
J2039.6–5618	PowerLaw	13.0 ± 0.6	2.17 ± 0.03		1517	8.59	c-MSP
	PLSuperExpCutoff	10.6 ± 0.7	1.61 ± 0.09	4.4 ± 0.8	1571		
J2043.8–4801	PowerLaw	3.6 ± 0.5	2.20 ± 0.08		189	5.85	
	PLSuperExpCutoff	2.0 ± 0.4	0.8 ± 0.4	1.8 ± 0.5	221		
J2112.5–3044	PowerLaw	13.5 ± 0.6	2.01 ± 0.03		2053	13.54	c-subhalo
	PLSuperExpCutoff	9.7 ± 0.6	1.1 ± 0.1	3.0 ± 0.4	2237		
J2131.1–6625	PowerLaw	5.1 ± 0.5	2.42 ± 0.08		243	4.12	
	PLSuperExpCutoff	4.0 ± 0.6	1.6 ± 0.3	2.3 ± 0.8	258		
J2133.0–6433	PowerLaw	5.4 ± 0.6	2.27 ± 0.07		283	6.31	c-subhalo
	PLSuperExpCutoff	3.6 ± 0.5	1.1 ± 0.3	1.7 ± 0.5	311		

Table 2 Source without Sufficient Curvature Significance

Source name	Spectral model	Flux (10^{-9} photon cm^{-2} s^{-1})	Γ	E_c (GeV)	TS	Signif_Curve (σ)
J0737.2–3233	PowerLaw	14 ± 1	2.53 ± 0.06		326	2.87
	PLSuperExpCutoff	13 ± 1	2.1 ± 0.2	3 ± 1	330	

Table 3 Sources without Clean Background

Source name	Spectral model	Flux density (10^{-12} photon cm^{-2} MeV^{-1} s^{-1})	Γ	E_0 (MeV)	Signif_Avg (σ)	Signif_Curve (σ)
J0456.2–6924	PowerLaw	0.88 ± 0.10	2.3	1057	9.9	3.6
J0816.1–5044	PowerLaw	2.40 ± 0.32	2.5	771	7.75	3.6
J0905.8–2127	PowerLaw	4.93 ± 0.75	2.7	477	6.6	3.3
J1256.1–5703	PowerLaw	5.16 ± 0.77	2.7	544	6.4	3.3
J1408.0–2924	PowerLaw	6.46 ± 0.87	2.7	419	7.4	3.3
J1820.4–3217	PowerLaw	1.00 ± 0.16	2.3	1011	6.2	3.3

Source name	Spectral model	Flux_Density (10^{-12} photon cm^{-2} MeV^{-1} s^{-1})	α	β	E_b (MeV)	Signif_Avg	Signif_Curve
J1128.6–5434	LogParabola	29.1 ± 3.4	2.56	0.94	336	8.5	4.2
J1557.0–4225	LogParabola	35.3 ± 3.7	2.33	0.55	369	11.5	4.4
J1729.7–2408	LogParabola	16.6 ± 1.7	2.47	0.40	567	11.7	4.4

2.3 Spectral Analysis

To obtain the γ -ray spectrum for each clean point-like source, we ran *glike* at the best-fit position determined. We evenly divided energy logarithmically from 0.1 to 300 GeV into 15 energy bands. We first modeled each source with a simple PL, with Γ fixed at the value derived from the above. The spectral data points were obtained, but only those with $\text{TS} > 4$ were kept. We secondly repeated the analysis using a PL with an exponential cutoff (PLE),

$$\frac{dN}{dE} = N_0 \left(\frac{E}{E_0} \right)^{-\Gamma} \exp \left(-\frac{E}{E_c} \right), \quad (3)$$

where E_c is the cutoff energy and $E_0 = 1$ GeV was set. The results from the two spectral models were compared, and the curvature significance *Signif_curve* was estimated from

$\text{Signif_curve} = \sqrt{2 \log(L_{\text{PLE}}/L_{\text{PL}})}$, where L_{PLE} and L_{PL} are the maximum likelihood values modeled with PLE and PL, respectively. The analysis shows that all the sources had significant curvature except one, J0737.2–3233. Its spectral results are given in Table 2, indicating that a PLE model is not significantly better than a PL one. In Figure 1, its spectrum is also shown. We excluded this source from our candidate list.

2.4 Variability Analysis

We performed temporal analysis of the LAT data for the 28 remaining sources. The time period was from 2008 August 4 23:59:59 to 2015 September 30 23:59:56

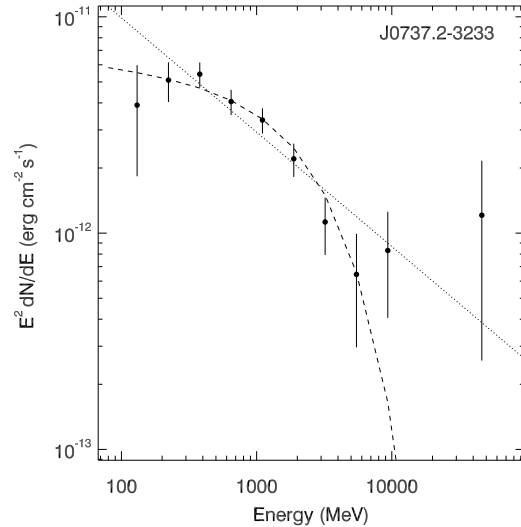


Fig. 1 γ -ray spectrum of J0737–3233. The dotted and dashed lines are the best-fit PL and PLE models, respectively.

(UTC) and we divided it into 30-day intervals. The PL model, with photon index fixed at the value obtained in Section 2.3, was used for conducting likelihood analysis in each time bin at the best-fit position of each source. We obtained the light curves and TS curves for the sources. Consistent with the results in the 3FGL, we did not find any significant flux variations in the light curves.

3 X-RAY DATA ANALYSIS

Possible X-ray counterparts of the 28 candidate MSPs were searched in archival X-ray observations. We uti-

lized publicly available X-ray observations from the *Swift*, *Chandra*, *XMM-Newton* and *Suzaku* satellites. Among the candidates, 26 of them were observed at least once with the above mentioned observatories, and we selected the longest-exposure observation among the available datasets. However, two sources (J1744.1–7619 and J2039.6–5618; Hui et al. 2015; Salvetti et al. 2015; Romani 2015) have been well studied in multi-wavelength and verified to likely be MSPs. These two sources were thus not included in this analysis. We used the HEASOFT package version 6.15.1 distributed by the High Energy Astrophysics Science Archive Research Center (HEASARC) for the analysis.

3.1 Data Analysis

3.1.1 *Swift* XRT analysis

The data for the candidate MSPs obtained with the *Swift* X-ray Telescope (XRT; Burrows et al. 2005) were downloaded from HEASARC. The unfiltered event files from Photon Counting (PC) mode observations were reduced using the XRTPipeline task and calibration files version 20150721 available in the *Swift* CALDB. The X-ray sources in the XRT images were detected from running the command DETECT available in the XIMAGE. We used a detection threshold of 3σ and considered only the X-ray sources within the 2σ *Fermi* error circle as the possible X-ray counterparts. The exact positions of the X-ray sources detected were estimated by using the XRTCEN-TROID task. For the possible counterparts, we extracted the source and background spectra from a circular region of radius $47''$ along with the ancillary response files (ARF) and response matrix files (RMF). If there were sufficient spectral counts to perform spectral modeling, we grouped the spectra using GRPPHA with a minimum of 20 counts per bin and adopted the χ^2 statistic. For the sources with limited net counts, we used the Cash Statistic (Cash 1979) for the spectral fitting.

For the detected X-ray sources, we tested the spectral models such as PL, blackbody (BBODY) and APEC, each combined with interstellar absorption. In all cases, we fixed the absorption column density (tbabs; Wilms et al. 2000) to the Galactic values (Kalberla et al. 2005). The spectral fitting results with an absorbed PL model are summarized in Table 4. In many cases, no X-ray source was detected, thus we estimated the 3σ upper limits on the count rates using the UPLIMIT command in XIMAGE. The upper limits were then converted into fluxes by using webPIMMS² (assuming an absorbed PL model

with $\Gamma = 1.7$ and the absorption column density of the Galactic value). The upper limits are listed in Table 5.

3.1.2 *Chandra* analysis

The *Chandra* observations were analyzed using the science threads of *Chandra* Interactive Analysis of Observations (CIAO) version 4.6 with CALDB version 4.6.1.1. The *Chandra* data were reprocessed with the CIAO tool CHANDRA.REPRO. We ran the CELLDETECT task on the reprocessed event files with a detection threshold of 3σ to detect the X-ray sources. The source and background regions were extracted from a circular region of radius $5'' - 10''$, and we performed the SPEXTRACT task in CIAO to generate the source and background spectra and the corresponding response files (ARF and RMF). The source spectra were grouped using GRPPHA with a minimum of 20 counts per bin, and the spectral fitting was performed with the χ^2 statistic. For low quality spectra, we used the Cash Statistic.

3.1.3 *XMM-Newton* analysis

We retrieved the observation data files from the *XMM-Newton* Science Archive and used the *XMM-Newton* Science Analysis Software (SAS) version 14.0 to analyze them. We performed standard data processing for the European Photon Imaging Camera (EPIC) pn (Strüder et al. 2001) and MOS (Turner et al. 2001) detectors with the EPCHAIN and EMCHAIN tools. The high particle background time intervals were excluded from the observations and only 0–4 pattern events from the pn and 0–12 from the two MOS detectors were selected. We ran the detection on the cleaned and filtered event files in the 0.3–10 keV energy range using the SAS task EDETECT_CHAIN. As mentioned in Section 3.1.1, we selected the X-ray sources within the 2σ *Fermi* error circles and extracted the source and background spectra from circular regions of radius $12'' - 30''$. The source and background spectra, together with response and ancillary response files, were obtained using the ESPECGET task. For each source, we fitted simultaneously the pn and MOS spectra using XSPEC version 12.8.1g. The spectral modeling was performed with either the χ^2 statistic or the Cash Statistic. The resulting spectral model parameters are given in Table 4.

3.1.4 *Suzaku* analysis

Suzaku (Mitsuda et al. 2007) observed the candidate J1946.4–5403 with its X-ray imaging spectrometer (XIS) on 2011 October 31 for an exposure time of 42.4 ks

² <http://heasarc.gsfc.nasa.gov/cgi-bin/Tools/w3pimms/w3pimms.pl>

Table 4 Log and Fitting Results of X-ray Sources in the Fields of the Candidate MSPs using a PL Model

Source	Data	ObsID	Exp (ks)	X-ray Source	R.A. (h:m:s)	Dec. (° :′ :″)	N_{H} (10^{21})	Γ	F_{X} (10^{-14})	χ^2/dof	GXR (G_{100})
(1)	(2)	(3)	(4)	(5)	(6)	(7)	(8)	(9)	(10)	(11)	(12)
J0802.3	<i>XMM</i>	0691980301	18.1	X1	8:02:16.56	-56:11:51.00	1.50	1.7(<i>f</i>)	$0.66^{+0.95}_{-0.00}$	11.4/4(C)	1333 (8.8)
				X2	8:02:08.64	-56:12:13.68	1.50	$2.14^{+0.93}_{-0.74}$	$2.62^{+1.47}_{-0.99}$	0.9/5 (C)	336
				X3	8:02:13.92	-56:13:21.36	1.50	$1.93^{+0.83}_{-0.72}$	$2.35^{+1.69}_{-0.99}$	2.3/4(C)	374
				X4	8:01:59.04	-56:11:24.00	1.50	$0.90^{+1.08}_{-0.98}$	$3.18^{+3.93}_{-1.82}$	0.2/2(C)	277
				X5	8:02:19.20	-56:14:37.32	1.50	$2.59^{+1.52}_{-0.95}$	$2.86^{+3.32}_{-1.28}$	2.2/2(C)	308
J0838.8	<i>Swift</i>	00041343002	4.2	X1	8:38:43.20	-28:27:01.45	1.39	$1.70^{+0.18}_{-0.18}$	$466.0^{+54.5}_{-51.4}$	15.1/14	2 (9.4)
J0933.9	<i>Chandra</i>	14813	43.6	X1	9:34:00.58	-62:33:52.44	2.04	4.05	—	25.9/7*	(12)
J0954.8	<i>Swift</i>	00031664001	3.6	X1	9:55:27.78	-39:47:49.84	1.35	$0.32^{+1.21}_{-1.35}$	$108.0^{+410.0}_{-76.2}$	1.4/3(C)	16 (17)
J1035.7	<i>XMM</i>	0692830201	24.9	X1	10:35:27.60	-67:20:15.36	1.80	$2.86^{+0.76}_{-0.64}$	$2.69^{+1.34}_{-0.92}$	11.7/14(C)	781 (21)
J1119.9	<i>XMM</i>	0742930101	73.6	X1	11:19:58.08	-22:04:57.00	0.37	$2.21^{+0.15}_{-0.15}$	$14.10^{+1.29}_{-1.27}$	45.8/33	128 (18)
				X2	11:20:01.68	-22:04:55.92	0.37	$1.70^{+0.31}_{-0.30}$	$5.24^{+1.32}_{-1.10}$	3.4/8	343
				X3	11:19:59.04	-22:03:15.48	0.37	$1.12^{+0.62}_{-0.70}$	$2.04^{+1.34}_{-0.82}$	3.3/3(C)	1607
J1624.2	<i>XMM</i>	0722940101	31.0	X1	16:24:09.84	-40:44:25.08	2.60	$-0.27^{+0.62}_{-0.81}$	$4.76^{+1.87}_{-1.58}$	4.8/7(C)	567 (27)
				X2	16:24:07.68	-40:44:37.32	2.60	$1.21^{+0.58}_{-0.56}$	$2.22^{+1.05}_{-0.78}$	9.2/6(C)	1216
				X3	16:24:02.16	-40:45:44.28	2.60	$1.41^{+0.44}_{-0.49}$	$2.56^{+0.94}_{-0.75}$	10.8/6(C)	1055
				X4	16:24:15.12	-40:47:12.48	2.60	$0.96^{+0.88}_{-0.92}$	$1.92^{+1.35}_{-1.06}$	8.8/8(C)	1406
				X5	16:24:09.36	-40:42:38.88	2.60	$1.69^{+0.80}_{-0.79}$	$0.98^{+0.65}_{-0.51}$	10.4/8(C)	2755
				X6	16:24:04.56	-40:47:20.76	2.60	$6.18^{+3.15}_{-2.80}$	$34.40^{+716.0}_{-31.3}$	8.2/8(C)	78
				X7	16:24:12.48	-40:47:57.12	2.60	$0.97^{+0.56}_{-0.58}$	$3.78^{+1.86}_{-1.42}$	4.9/8(C)	714
				X8	16:24:26.16	-40:45:40.32	2.60	$1.78^{+1.42}_{-1.14}$	$1.16^{+0.89}_{-0.64}$	15.7/7(C)	2328
J1626.2	<i>Chandra</i>	17249	100.0	X1	16:26:48.49	-24:28:38.91	1.34	$1.08^{+0.60}_{-0.55}$	$3.43^{+0.86}_{-0.74}$	7.5/6(C)	845 (29)
				X2	16:26:40.49	-24:27:15.13	1.34	0.56	—	59.0/17*	
				X1	16:26:48.41	-24:28:36.93	1.34	$0.68^{+0.75}_{-0.73}$	$2.13^{+1.13}_{-0.82}$	9.6/6(C)	1361
		637	97.7	X2	16:26:40.48	-24:27:14.60	1.34	0.63	—	23.5/9*	
J1946.4	<i>Suzaku</i>	706026010	42.4	X1	19:46:33.82	-54:02:37.23	0.37	$1.29^{+0.29}_{-0.28}$	$12.7^{+2.36}_{-2.26}$	23.7/18	72 (9.2)
J2112.5	<i>XMM</i>	0672990201	33.8	X1	21:12:32.16	-30:44:04.92	0.66	$2.20^{+0.73}_{-0.59}$	$1.48^{+0.78}_{-0.54}$	7.7/5	1284 (19)

Notes: * denotes the cases where the reduced $\chi^2 > 2$ and we tried other spectral models. Column (1) Source name; Col. (2) Data; Col. (3) ID of the observations; Col. (4) Exposure time in ks for each observation; Col. (5) X-ray sources in the 2σ error circle; Cols. (6)–(7) Right Ascension (R.A.; J2000.0) and Declination (Dec.; J2000.0); Col. (8) Galactic absorption column density in units of cm^{-2} ; Col. (9) Photon index; Col. (10) Unabsorbed flux in 0.3–10 keV band in units of $\text{erg cm}^{-2} \text{s}^{-1}$; Col. (11) χ^2/dof value for the model, where Cash Statistic is indicated by C; Col. (12) γ -ray to X-ray flux ratios (GXR) for each candidate MSP with X-ray sources detected in the field, where the γ -ray 0.1–100 GeV flux (G_{100}) of each candidate MSP, in units of $10^{-12} \text{ erg cm}^{-2} \text{ s}^{-1}$, is given in parentheses.

Table 5 X-ray Flux Upper Limits for 14 Candidate MSPs

Src Name	R.A. (°)	Dec. (°)	Data	ObsID	Exp Time	CR ($\times 10^{-3}$)	N_{H} ($\times 10^{20}$)	$F_{\text{X}}^{\text{upper}}$ ($\times 10^{-13}$)	$G_{100}/10^{-12}$ ($\text{erg cm}^{-2} \text{ s}^{-1}$)	$G_{100}/F_{\text{X}}^{\text{upper}}$
(1)	(2)	(3)	(4)	(5)	(6)	(7)	(8)	(9)	(10)	(11)
J0048.1–6343	12.21070306	-63.76885597	<i>Swift</i>	00047132001	3099	< 3.27	1.97	< 1.34	1.7	> 13
J1231.6–5113	187.9228875	-51.2445342	<i>Swift</i>	00041384001	3602	< 2.09	13.90	< 1.16	12	> 103
J1400.2–2413	210.0116122	-24.2486119	<i>Swift</i>	00047217004	2186	< 7.56	5.33	< 3.51	3.4	> 9.7
J1539.2–3324	234.8356327	-33.41744465	<i>Swift</i>	00048054023	15084	< 0.81	9.06	< 0.41	1.0	> 24
J1544.1–2555	236.0585575	-25.9120224	<i>Swift</i>	00085021004	993	< 11.80	11.00	< 6.24	7.9	> 13
J1649.6–3007	252.4595489	-30.1831453	<i>Swift</i>	00085034001	4155	< 5.35	15.90	< 3.08	7.1	> 23
J1702.8–5656	255.6861421	-56.91435142	<i>Swift</i>	00041424001	1214	< 6.39	11.30	< 3.40	37	> 108
J1753.6–4447	268.3488964	-44.76971147	<i>Swift</i>	00047264001	1567	< 8.63	13.20	< 4.75	7.6	> 16
J1757.7–6030	269.4143008	-60.55432813	<i>Swift</i>	00047265005	1994	< 4.97	7.19	< 2.42	3.7	> 15
J1808.3–3357	272.1154608	-33.86901995	<i>Swift</i>	00047271002	7123	< 3.09	18.10	< 1.84	8.7	> 47
J1831.6–6503	277.7440476	-65.06402308	<i>Swift</i>	00047281002	1704	< 7.50	6.70	< 3.61	3.7	> 10
J2043.8–4801	310.9822976	-48.02857435	<i>Swift</i>	00047307004	1116	< 10.20	2.83	< 4.35	3.6	> 8
J2131.1–6625	322.7121318	-66.40198989	<i>Swift</i>	00085130006	845	< 9.51	2.44	< 3.99	4.9	> 12
J2133.0–6433	323.3171713	-64.53428129	<i>Swift</i>	00047316004	3357	< 4.98	3.09	< 2.15	5.1	> 23

Notes: Column (1) Source name; Cols. (2)–(3) Right Ascension (R.A.; J2000.0) and Declination (Dec.; J2000.0) of each source; Col. (4) Data; Col. (5) ID of observation used in the analysis; Col. (6) Exposure time in seconds for each observation; Col. (7) 3σ upper limit of count rate in unit of counts s^{-1} ; Col. (8) Galactic absorption column density in cm^{-2} . Col. (9) 3σ upper limit of flux in 0.3–10 keV band in units of $\text{erg cm}^{-2} \text{ s}^{-1}$; Col. (10) γ -ray 0.1–100 GeV flux; Col. (11) Lower limit on the γ -ray to X-ray flux ratio.

(Observation ID: 706026010). We cleaned and calibrated the unfiltered event files (XIS data) using standard filtering criteria with the specific HEADAS tool AEPipeline and calibration files (version 20130110) available in the *Suzaku* CALDB. The source, shown in Figure 2, and background regions were taken from a circular region of radius $70''$ and the spectra, response matrices, and ancillary response files were generated using XSELECT for XIS0, XIS1 and XIS3. The front illuminated (FI) CCD spectra, XIS0 and XIS3, were added using the FTOOL ADDASCASPEC. The co-added spectrum was then grouped to minimum counts of 20 and χ^2 statistics was used for the spectral fitting.

3.2 Individual Sources

Among the 24 sources studied here, 10 of them have one or more X-ray sources within the 2σ *Fermi* error circle and the rest of them do not. In the following sections, we discuss the properties of individual sources which we fitted with spectral models other than a PL.

3.2.1 J0838.8–2829

We have detected only one source, named X1, for J0838.8–2829 in the *Swift* observation (ObsID: 00041343002). We examined the spectrum with an absorbed PL model and the spectral results are given in Table 4. We then added a blackbody component (BBDY) to the PL and the spectral fit was improved marginally ($\Delta\chi^2 \sim 3.7$ for 2 degrees of freedom (dof) at a confidence level of $\sim 82\%$). The spectral parameters, $kT = 0.14_{-0.09}^{+0.06}$ keV, $\Gamma = 1.46_{-0.30}^{+0.26}$ and $F_X = 5.78_{-4.40}^{+4.42} \times 10^{-13}$ erg cm $^{-2}$ s $^{-1}$ ($\chi^2/\text{dof} = 11.4/12$), are consistent with those of typical MSPs (Zavlin 2007; Marelli 2012).

3.2.2 J0933.9–6232

The 43 ks *Chandra* ACIS-S observation detected only one X-ray source (X1) in the field of J0933.9–6232. The absorbed PL model did not provide a statistically acceptable fit ($\chi^2/\text{dof} = 25.9/7$) for the spectrum of this source. We also tried different models such as a BBDY or an APEC. In all cases, the spectral fits were worse ($\chi_r^2 > 2$). Thus, we used a two-component model such as the PL plus APEC model. This model gave an acceptable fit, $\chi^2/\text{dof} = 8.6/5$, from which $\Gamma = 2.22_{-2.87}^{+1.99}$, $kT = 0.90_{-0.14}^{+0.11}$ keV and $F_X = 1.54_{-0.68}^{+3.84} \times 10^{-14}$ erg cm $^{-2}$ s $^{-1}$. We note that Saz Parkinson et al. (2016) also analyzed the same observation and reported

the detection of X1. However, only the PL model was considered in their analysis.

3.2.3 J1119.9–2204

The field of J1119.9–2204 was observed by *Swift* on multiple occasions (ObsID: 00049351025 and 00049351021) and Hui et al. (2015) have reported their data analysis. Two sources were detected with *Swift*. *XMM-Newton* observed the field on 2014 June 14 for a total exposure of ~ 73.6 ks (Obs. ID: 0742930101). In the *XMM-Newton* observation, one additional source was detected. Among them, the source X1 had enough spectral counts, allowing detailed spectral modeling. We initially fitted the spectrum with an absorbed PL model which provides an acceptable fit, with $\Gamma = 2.21 \pm 0.15$ ($\chi^2/\text{dof} = 45.8/33$). The addition of a blackbody component to the PL improved the spectral fit significantly, $\Delta\chi^2 \sim 12.5$ for 2 dof at a confidence level of $> 99\%$. The best-fit parameters are $kT = 0.20 \pm 0.03$ keV, $\Gamma = 1.34_{-0.78}^{+0.62}$ and $F_X = 5.42_{-2.50}^{+1.65} \times 10^{-14}$ erg cm $^{-2}$ s $^{-1}$. The parameters of X1 were consistent with those of typical MSPs (Zavlin 2007; Marelli 2012), while the emission from each of the other two sources (X2 and X3) favors a non-thermal case (Table 4).

3.2.4 J1624.2–4041

The field of J1624.2–4041 was observed by *XMM-Newton* for an exposure of 31 ks on 2013 August 14 (ObsID: 0722940101). We identified eight possible X-ray sources and analyzed the spectra of these sources with an absorbed PL model. All the sources were fitted well except the source X6 (See Table 4). For X6, the PL model could provide a statistically acceptable fit ($C = 8.2$ for 8 dof), but resulted in an unphysically large photon index, $\Gamma = 6.18_{-2.80}^{+3.15}$. Therefore, the non-thermal case is not favored for this source. We tested an absorbed blackbody model. With N_H fixed at the Galactic value 2.60×10^{21} cm $^{-2}$, the model yielded a temperature of $kT = 0.12_{-0.03}^{+0.06}$ keV with $C = 8.8$ for 8 dof, which indicates a possible thermal origin for this source.

3.2.5 J1626.2–2428c

The deep *Chandra* ACIS-I observations (ObsID: 17249 and 637; exposure times of 100.1 and 97.7 ks respectively) conducted on 2014 October 06 and 2000 May 15 covered the field of J1626.2–2428c. We reprocessed these long observations using standard tools in CIAO and identified two X-ray sources. The emission from the first source (X1) can be fitted by a PL model in both obser-

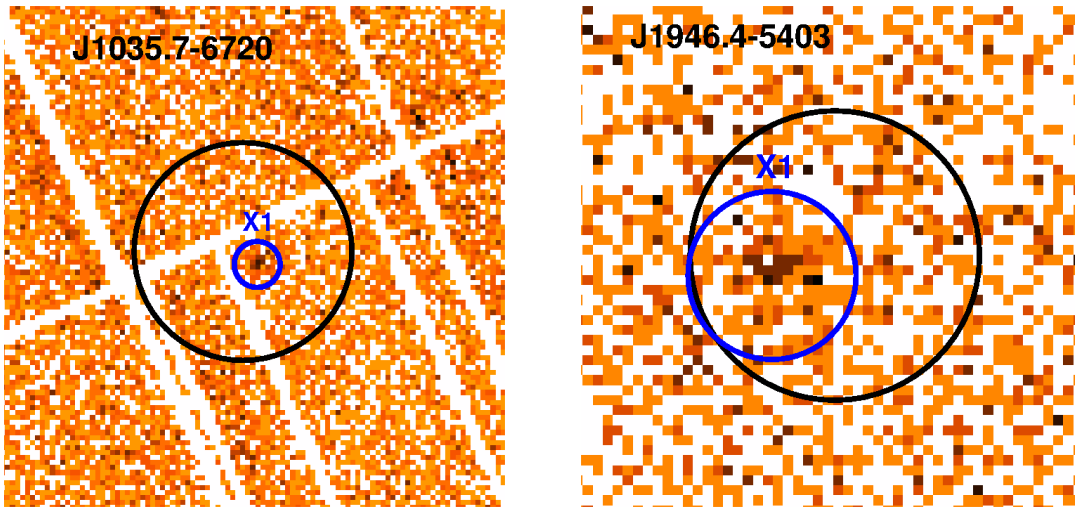


Fig. 2 Image fields of J1035.7–6720 (*left*) and J1946.4–5403 (*right*) as obtained from the *XMM-Newton* EPIC pn and *Suzaku* XIS, respectively (see Table 4). The black circles indicate the 2σ *Fermi* error circles and the candidate X-ray counterparts are marked by blue circles.

vations. The PL index and flux are constant within the uncertainties (see Table 4). The spectra of the source X2 cannot be described by a single component model (PL, blackbody or APEC) or two-component models (such as a PL plus blackbody or a PL plus APEC). Thus, we attempted a broken PL model for both observations. For the 2014 October observation, the broken PL fit results in $\Gamma_1 = -1.85^{+0.87}_{-1.13}$ below the break energy $E_{\text{break}} = 3.08^{+0.27}_{-0.21}$ and $\Gamma_2 = 2.22^{+0.66}_{-0.55}$ above the break energy with $\chi^2/\text{dof} = 19.2/15$. For the 2000 May observation, the broken PL provided an acceptable fit with $\Gamma_1 < -0.31$, $E_{\text{break}} = 2.70^{+0.31}_{-0.93}$ and $\Gamma_2 = 1.87^{+0.58}_{-1.42}$ ($\chi^2/\text{dof} = 5.3/7$). These spectral parameters have been widely reported for high-redshift radio loud quasars (Fabian et al. 2001; Yuan et al. 2006; D’Ammando & Orienti 2016). Thus from the X-ray properties we can say that X2 is probably a background quasar.

4 RESULTS AND DISCUSSION

We have analyzed the *Fermi* LAT data for another 38 unassociated sources selected from 3FGL for identifying candidate MSPs. From the analysis, 29 clean point-like sources were found, while one of them, J0737.3–3233, was excluded as a candidate MSP since its spectrum does not show significant curvature. Among the remaining 28 sources, J2043.8–4801 appears to possibly have two components in its spectrum, which is shown in Figure 3. We examined its TS maps and it is consistent with being a point source. The TS maps at low and high energy ranges (e.g., 0.1–1.0 GeV and 1.0–300 GeV, respectively) were also calculated, but no evidence was found for having an

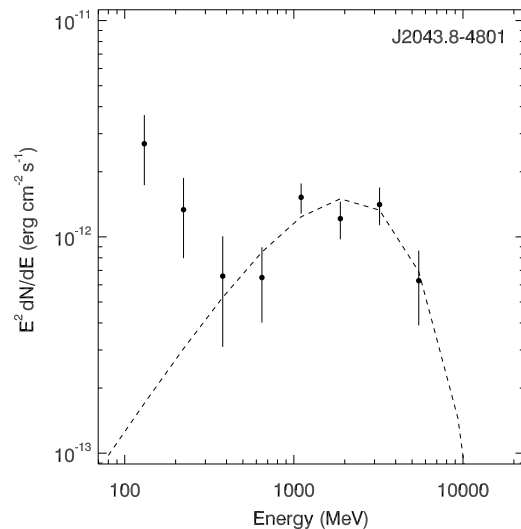


Fig. 3 γ -ray spectrum of J2043.8–4801. The dashed curve indicates the best-fit PLE model, which does not describe the spectral data points well, as the spectrum probably has two components.

additional source at the source position. Such a source needs further studies for investigating the possible nature of its emission.

Five of the 28 sources have already been identified as likely pulsars from radio searches or γ -ray data analysis: J0514.6–4406 is probably the counterpart to PSR J0514–4407 (but with a spin period of 302.2 ms; Bhattacharyya et al. 2016); J1946.4–5403 is an MSP in a binary with a 3 hour orbital period (a possible black widow system; Camilo et al. 2015); J1035.7–6720,

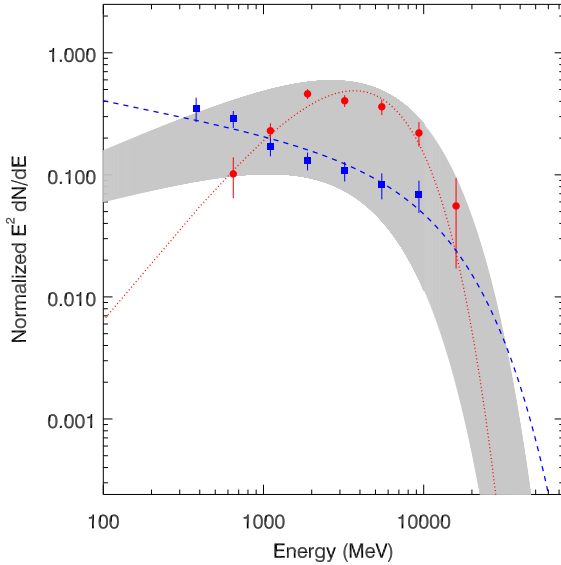


Fig. 4 γ -ray spectra of J1539.2–3324 (red dots) and J1626.2–2428c (blue squares), with the red dotted and blue dashed curves being the best-fit PLE models, respectively. The grey area indicates the 3σ region of the best-fit spectral model derived from 39 known γ -ray MSPs listed in Abdo et al. (2013).

J1624.2–4041 and J1744.1–7619 have been found with γ -ray pulsations (Camilo et al. 2015). Optical and/or X-ray observations have also helped identification of the possible MSP nature for several sources: J2039.6–5618 is very likely a redback MSP system with an orbital period of ~ 5.4 hours (Salvetti et al. 2015; Romani 2015); J0933.9–6232 (Saz Parkinson et al. 2016 and this work) and J1119.9–2204 (2FGL J1120.0–2204; Guillemot et al. 2012; Hui et al. 2015; this work) were found to have possible X-ray counterparts and suggested to likely be MSPs. These sources are marked as ‘c-MSP’ in Table 1. In addition as we note in Camilo et al. (2015), 13 of our candidates are listed as their targets for searching for radio pulsars, although thus far no radio pulsation signals have been found. These studies strongly support our data analysis results.

MSPs generally have γ -ray spectra with Γ and E_c in the ranges of 0.4–2.0 and 1.1–5.4 GeV respectively (see Abdo et al. 2013 for details). Recently, Xing & Wang (2016) have analyzed the spectra of 39 MSPs listed in the second *Fermi* γ -ray pulsar catalog and obtained the spectral ranges of $\Gamma = 1.43$ –1.64 and $E_c = 3.00$ –4.65 GeV (3σ) from fitting their spectra with a PLE model. If we consider the Γ range, which is relatively well determined, five sources have their Γ values out of the range, especially the sources J1539.2–3324 and J1626.2–2428c

that have the parameters of

$$\Gamma = 0.4 \pm 0.2, \quad E_c = 2.2 \pm 0.3 \text{ GeV}$$

and

$$\Gamma = 2.3 \pm 0.1, \quad E_c = 10 \pm 5 \text{ GeV},$$

respectively.

For this reason, we tentatively suggest that the five sources are not MSPs, marked with ‘N’ in Table 1. The spectra of J1539.2–3324 and J1626.2–2428c are shown as an example in Figure 4. The first source has been searched in X-ray data as a candidate MSP but no possible counterpart was found (Hui et al. 2015) and is listed as a candidate blazar in the *Fermi* third AGN catalog (Ackermann et al. 2015b). The second one, with a larger Γ value, is possibly associated with the blazar PMN J1626–2426 (Ackermann et al. 2015b). However if this is the case, none of the two X-ray sources reported in Section 3.2.5 would be the counterpart because of the position mismatch (Griffith & Wright 1993).

On the other hand, the other three ‘N’ sources include J0933.9–6232, which is considered to be a promising MSP candidate. Whether the Γ range derived in Xing & Wang (2016) is a reliable criterion for excluding non-MSP sources will be tested, once the nature of such ‘N’ sources is identified.

We have analyzed archival X-ray data that were available for 24 of our selected candidate MSPs. In the fields of 10 of them, at least one object was detected. For the likely pulsars J1035.7–6720, J1624.2–4041 and J1946.4–5403, the spectra of the objects are consistent with being a non-thermal PL with photon indices of ~ 1 –3. In addition, the flux ratios between their γ -ray 0.1–100 GeV flux (G_{100}) and the X-ray fluxes of the detected objects are in a range of ~ 100 –1000, also consistent with that of most known γ -ray pulsars (Abdo et al. 2013). Both properties suggest that the X-ray objects, particularly in the fields of J1035.7–6720 and J1946.4–5403 (containing only one object), are likely the counterparts. While detailed X-ray studies of the objects in the fields of J0933.9–6232 and J1119.9–2204 have been previously conducted, our analysis of the different sets of X-ray data has confirmed the previous results. In order to identify the X-ray objects in each source field and possibly verify their pulsar nature, optical observations of them used in searching for variability can be the next step. Nearly 70% of the *Fermi* γ -ray MSPs are in binaries (e.g., Abdo et al. 2013; Camilo et al. 2015).

Since the companions of MSP binaries are irradiated by pulsar winds, they may show significant orbital modulation at optical bands, thus revealing their pulsar binary nature (e.g., Romani 2015). Finally, 14 of our selected

candidates were not detected with any X-ray objects in their fields, the reason for which is probably because the X-ray observations were not sufficiently deep. The lower limits on the γ -ray-to-X-ray flux ratios are only as large as > 100 (see Table 5). Deep X-ray observations are needed in order to find X-ray objects, thus allowing further multi-wavelength studies.

As a summary for this systematic study, we have selected 101 sources from the *Fermi* 3FGL un-associated sources based on properties of known γ -ray MSPs and conducted detailed LAT data analysis for 77 of them that were detected with a significance of $\geq 6\sigma$. Our analysis indicates that 52 sources are point-like without strong background contamination and their emission is well described by a PLE model. A few of the 52 sources have already been studied at multiwavelengths and shown to be likely pulsars. We consider the remaining ones as good candidate MSPs for follow-up identification studies. For 44 of these candidates, we have conducted analysis of the archival X-ray observations. We have obtained spectral properties of the X-ray objects detected in the fields of 14 candidates, and derived flux upper limits for the other 30 candidates that did not have any X-ray objects detected in their fields (Paper I and this work). The X-ray study results generally support their pulsar nature. Finally, we note that approximately 10 of our candidates (excluding those already identified as pulsars) are also listed as promising dark matter subhalo candidates (marked with c-subhalo in Table 1; see also Paper I) in Bertoni et al. (2015). This possibility certainly makes the candidates more interesting targets for follow-up studies.

Acknowledgements This research made use of the High Performance Computing Resource in the Core Facility for Advanced Research Computing at Shanghai Astronomical Observatory. This research was supported by the National Program on Key Research and Development Project (Grant No. 2016YFA0400804), the Strategic Priority Research Program “The Emergence of Cosmological Structures” of the Chinese Academy of Sciences (Grant No. XDB09000000), and the National Natural Science Foundation of China (11373055 and 11633007). Z.W. acknowledges the support by the CAS/SAFEA International Partnership Program for Creative Research Teams; J.V. by the Chinese Academy of Sciences President’s International Fellowship Initiative (CAS PIFI, Grant No. 2015PM059); and Y.X. by the Shanghai Natural Science Foundation for Youth (13ZR1464400) and the National Natural Science Foundation of China for Youth (11403075).

References

- Abdo, A. A., Ackermann, M., Ajello, M., et al. 2010, *ApJS*, 188, 405
- Abdo, A. A., Ajello, M., Allafort, A., et al. 2013, *ApJS*, 208, 17
- Acero, F., Ackermann, M., Ajello, M., et al. 2015, *ApJS*, 218, 23
- Ackermann, M., Ajello, M., Atwood, W. B., et al. 2015a, *ApJ*, 810, 14
- Ackermann, M., Ajello, M., Atwood, W. B., et al. 2015b, *ApJ*, 810, 14
- Atwood, W. B., Abdo, A. A., Ackermann, M., et al. 2009, *ApJ*, 697, 1071
- Bertoni, B., Hooper, D., & Linden, T. 2015, *J. Cosmol. Astropart. Phys.*, 12, 035
- Bhattacharyya, B., Cooper, S., Malenta, M., et al. 2016, *ApJ*, 817, 130
- Burrows, D. N., Hill, J. E., Nousek, J. A., et al. 2005, *Space Sci. Rev.*, 120, 165
- Camilo, F., Kerr, M., Ray, P. S., et al. 2015, *ApJ*, 810, 85
- Cash, W. 1979, *ApJ*, 228, 939
- Dai, X.-J., Wang, Z.-X., Vadakkumthani, J., & Xing, Y. 2016, *RAA (Research in Astronomy and Astrophysics)*, 16, 97
- D’Ammando, F., & Orienti, M. 2016, *MNRAS*, 455, 1881
- Fabian, A. C., Celotti, A., Iwasawa, K., et al. 2001, *MNRAS*, 323, 373
- Griffith, M. R., & Wright, A. E. 1993, *AJ*, 105, 1666
- Guillemot, L., Freire, P. C. C., Cognard, I., et al. 2012, *MNRAS*, 422, 1294
- Hui, C. Y., Park, S. M., Hu, C. P., et al. 2015, *ApJ*, 809, 68
- Kalberla, P. M. W., Burton, W. B., Hartmann, D., et al. 2005, *A&A*, 440, 775
- Marelli, M. 2012, arXiv:1205.1748
- Mattox, J. R., Bertsch, D. L., Chiang, J., et al. 1996, *ApJ*, 461, 396
- Mitsuda, K., Bautz, M., Inoue, H., et al. 2007, *PASJ*, 59, 1
- Muslimov, A. G., & Harding, A. K. 2004, *ApJ*, 606, 1143
- Romani, R. W. 2015, *ApJ*, 812, L24
- Salvetti, D., Mignani, R. P., De Luca, A., et al. 2015, *ApJ*, 814, 88
- Saz Parkinson, P. M., Xu, H., Yu, P. L. H., et al. 2016, *ApJ*, 820, 8
- Strüder, L., Briel, U., Dennerl, K., et al. 2001, *A&A*, 365, L18
- Turner, M. J. L., Abbey, A., Arnaud, M., et al. 2001, *A&A*, 365, L27
- Wilms, J., Allen, A., & McCray, R. 2000, *ApJ*, 542, 914
- Xing, Y., & Wang, Z. 2016, *ApJ*, 831, 143
- Yuan, W., Fabian, A. C., Worsley, M. A., & McMahon, R. G. 2006, *MNRAS*, 368, 985
- Zavlin, V. E. 2007, *Ap&SS*, 308, 297